Int J Adv Manuf Technol (2015) 79:65–79
DOI 10.1007/s00170-015-6801-3

ORIGINAL ARTICLE

A predictive hybrid force modeling in turning: application to stainless steel dry machining with a coated groove tool

Christophe Czarnota · Fousseny Koné · Badis Haddag · Mohammed Nouari

Received: 9 January 2014 / Accepted: 11 January 2015 / Published online: 28 January 2015

Abstract This paper presents an hybrid numerical/analytical modeling for estimation of cutting forces in machining process. The approach dedicated to predict 3D cutting forces are based on a chip flow direction modeling coupled with plane strain numerical simulations. An equivalent uncut chip thickness, deduced from the chip flow direction, is used as an input parameter in the 2D FEM. Resulting 2D numerical cutting forces are thus obtained from FEM, and knowing the chip flow direction, tangential, radial, and feed forces are calculated. Cutting forces derived from the proposed approach are compared to experiments when machining 304L austenitic steel with a groove-coated tool under dry condition. To take into account the complex groove geometry, the real shape of the cutting tool used in experiments has been captured by means of a digitization procedure, and thus implemented in 2D plane strain numerical simulations. The approach is applied to the case of stainless steel turning over a great range of cutting conditions. Two chip flow direction modelings are considered for the cutting force decomposition where it is shown the good predictive capabilities of the proposed approach.

Keywords Cutting force · Hybrid modeling · Numerical simulation · Turning 304L · Coated groove tools

C. Czarnota (✉)
Université de Lorraine Laboratoire d'Étude des Microstructures et de Mécanique des Matériaux LEM 3 - UMR CNRS 7239
Ile du Saulcy, 57045 Metz–Cedex 01, France
e-mail: christophe.czarnota@univ-lorraine.fr

F. Koné
Université de Cocody / Institut Pédagogique National de l'Enseignement Technique et Professionnel IPNETP,
08 BP 2098 Abidjan 08, Côte d'Ivoire
e-mail: foussenykone@gmail.com

B. Haddag · M. Nouari
Université de Lorraine Laboratoire d'Énergétique et de Mécanique Théorique et Appliquée LEMTA - UMR CNRS 7563 GIP-InSIC,
27 rue d'Hellieule 88100 Saint-Dié-des-Vosges, France

B. Haddag
e-mail: badis.haddag@univ-lorraine.fr

M. Nouari
e-mail: mohammed.nouari@univ-lorraine.fr

1 Introduction

Modeling cutting forces may be useful to control and ensure proper monitoring of machining operation, or to achieve process optimization. Cutting can be performed without coolant, which is nowadays an economical and ecological challenge, particularly when machining stainless steels known as difficult-to-cut materials. Therefore, predicting cutting forces will be helpful to determine optimal cutting conditions, so that the tool life and the quality of the machined piece will be improved. Furthermore, cutting forces prediction also helps in the formulation of simulation models used in machining databases. These models may be analytical, empirical, numerical, or a combination and usually lead to relationships between cutting conditions and cutting forces. In the present study, we focus on a hybrid analytical/numerical modeling of 3D cutting forces based on an analytical chip flow angle estimation, a 3D-digitization/2D-profile extraction and 2D numerical simulations. The approach is compared to experimental data obtained when dry machining of AISI 304L stainless steel with a carbide-coated grooved tool.

From early fundamental 2D machining developments in the 40s (e.g., [1]) to recent 3D finite element calculations of complex processes with complex tools [2, 3],

numerous authors developed modelings able to predict cutting forces in diverse machining processes. These modelings are often coupled with studies of the chip flow direction, an important characteristic which influences the chip control. It is also an essential information to calculate cutting force components. In this respect, Merchant [1], studying the oblique cutting with a straight-edge tool, proposed a model based on geometrical considerations. In his work, the chip flow angle involved the chip thickness ratio and the inclination angle and cutting forces in 2D was computed from an energetic point of view. A common used model is attributed to Stabler [4] who suggested that the chip flow angle is equal to the inclination angle. Later, the same author [5] introduced a correction factor whose values depend on the workpiece material and cutting conditions. The rake angle was shown to have a significant role on the chip flow direction later in the work of Russell and Brown [6] who established an empirical relationship revealing better agreement with experimental data. Several models have been developed for nose radius tool such as the Colwell's one [7]. Based on geometrical considerations, the author defined the chip flow direction orthogonal to the segment joining the two end points of the uncut chip cross-section area. This approach was found to satisfy only the case of zero tool inclination and rake angles. Thus, Wang and Mathew [8] proposed an approach based on the discretization of the cutting edge. In the course of the derivation, the authors introduced an equivalent cutting edge and defined the chip flow direction with respect to this edge using the Stabler's flow rule. Wang [9] revisited the study by considering a local inclination angle and getting away from the concept of an equivalent cutting edge.

Jawahir and co-authors have done considerable works on the modeling of chip flow angle and machining predictions, including analytical, experimental, or finite element means. In the work of Jawahir and Wang [10], the authors offer a precise survey in the field of predictive models and optimization techniques for turning and milling operations. A part of these investigations is based on the equivalent toolface approach. Within the framework of Jawahir et al. [11], dealing with the prediction of the failure of a groove tool, an "imaginary" flat tool was introduced so as to be equivalent to a groove tool for a given set of cutting conditions. This procedure needs experimental measurements and a flat-tool cutting force predictive modeling is involved in an iterative procedure. Once the equivalent toolface is determined, contact lengths, stresses, strains, temperatures, forces, etc. can be computed. Other studies dealing with grooved tools have been conducted and have led to empirical relationships describing cutting forces. Fang and Wu [12] have considered a comparative experimental study of high-speed machining of Ti-6Al-4V and Inconel 718 and proposed power-law relationships to relate cutting forces to cutting parameters (cutting velocity, feed rate, and width of cut). In a recent work, Koné et al. [13] also identified power-law regression relations for the tangential and feed force components but used a two-exponential terms law to describe the radial force component dependencies. In this last work, the tool/workpiece combination was the same as that considered in the present work. Other relevant works dealing with grooved tools have been done by Deshayes [14] and Pereira et al. [15]. The first author studied, through experimental/numerical approach, different geometries of carbide grooved inserts (various complex chip breakers) when machining a medium carbon steel. In the course of his finite element approach, Deshayes [14] adopted an equivalent flat rake face tool where normal rake angle can vary from large negative to large positive values, depending on the considered geometry. Pereira et al. [15] analyzed the impact of the chip breaker on chip control as well as its significant influence on cutting forces, surface integrity, wear, and tool life. The authors have mentioned the necessity of correcting chip breaker type application on cutting conditions which generate an ideal chip flow pattern and, consequently, decreasing the cutting force.

It can be also found in the literature analyzes using numerical simulations and dealing with grooved cutting tools on machining operations. Beyond these studies, there are those performed by Yen et al. [16] regarding the effect of the edge preparation upon chip formation, cutting forces,and process parameters in orthogonal cutting. The authors underlined the marked effect of the chamfer angle on cutting forces which were shown to increase as the chamfer angle or width is increased. Koné et al. [17] emphasized, through 2D numerical simulations of a 316L stainless steel with a coated carbide tool, that the cutting tool geometry and thermal properties (defined by the coatings sequence) may have an important impact on the pressure and the temperature at the tool-chip interface, and thus greatly influence cutting forces. Adetoro and Wen [3] adopted a numerical approach to predict cutting forces in flat-end milling process. They developed a 2D ALE model to estimate the average and instantaneous cutting force components. Based on their model, cutting force components were expressed as functions of the uncut chip thickness, which varies during cutting. Their model was successfully validated with a comparison between numerical and experimental results. 3D numerical studies were also performed, such as those of Soo et al. [18] who developed a 3D finite element model of the ball nose end milling process. Another interesting numerical studies were performed by Özel [19], who studied the influence of edge micro-geometry on forces, stresses, friction, and tool wear in PcBN tooling, when machining AISI 4340 alloy steel. The author who performed cutting experiments and 3D finite element investigations showed that

variable micro-geometry insert edge design reduces the heat generation and stress concentration along the tool cutting edge significantly. He also illustrated that it induces less plastic strain on the machined workpiece. All of these ingredients, computed from numerical simulations, have a direct influence on the cutting forces.

Numerous analyzes have been conducted in the field of chip flow direction and cutting force predictions with more or less accuracy and involving for a given number of them, more or less complexity. The purpose of the present work is to propose a relative easy implementing approach to address complex tool geometry and cutting forces predictions, with no need in advance of experimental data. This is done by proposing a hybrid 2D-3D numerical predictive approach dedicated to estimate cutting forces in turning with complex tool geometries. Adopting numerical simulations with the aim to account for physical or empirical ingredients involving a great number of fundamental parameters (workpiece and tool behavior, contact formulation, coatings effects…) seems to be an issue to a better comprehensive of machining processes and to develop an accurate cutting force predictive modeling. However, this strategy appears to be time consuming especially when dealing with 3D processes such as turning operations. Plane strain orthogonal cutting approaches have been considered several times as a good approximation of the turning process under some restrictive conditions. In the present work, similar approach is adopted, but with a try to adjust the uncut chip thickness (input data in numerical calculations) to cutting conditions and to limit uncertainties that may arise from the real tool geometry. To this end, we have used a 3D-digitization system to capture the insert profile from which an accurate 2D-section is obtained. Then, numerical simulations were performed with the software DEFORM 2D and the uncut chip thickness deduced from the chip flow angle estimation. The paper is organized as follows. Section 2 describes the proposed approach illustrated with a synoptic diagram where the flexibility of the modeling is highlighted. In this work, one fundamental need is determining the chip flow direction which is computed here from two modelings available in the literature. Both are briefly reminded in the first section. The approach is applied to predict cutting forces from conducted experiments on a wide range of cutting conditions. Section 3 is dedicated to the description of experiments and obtained results. Section 4 deals with the 3D digitization procedure applied to capture the complex grooved tool geometry corresponding to the one used in experiments. From the acquired numerical 3D, a 2D section is extracted that serves as an input data in numerical simulations. Finite element aspects (material parameters, mesh, boundary conditions) and identified regression relationships are further addressed in Section 5. The last section is dedicated to measure the validity of the proposed approach by a comparison with experimental cutting forces.

2 Hybrid modeling

The aim of the proposed approach is to predict 3D cutting forces from 2D numerical simulations. This was achieved with the use of the chip flow angle (CFA) from which an equivalent uncut chip thickness was deduced. Descriptions and equations relative to the chip flow direction are limited here to the case of straight turning, but can be adapted to other machining processes with more general cutting conditions. A synoptic diagram is first presented and described, then two modelings of chip flow angle are briefly reminded: the Wang's based modeling [9], denote by **W**-model in the following, and the Colwell's based modeling [7], denoted by **C**-model in the following.

2.1 Basic equations and synoptic diagram

The 2D/3D model is based on the definition of an equivalent undeformed chip thickness h_{eq} deduced from knowing the CFA. The overall adopted strategy is embedded in a synoptic diagram shown in Fig. 1 where seven steps are defined.

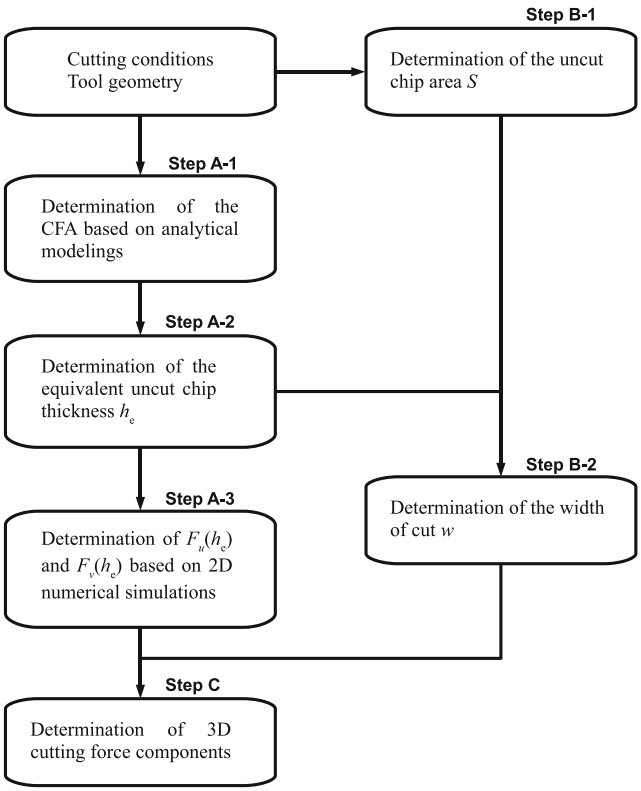

Fig. 1 Synoptic diagram of the proposed 2D-3D cutting force components modeling

- **Step A-1** Knowing cutting conditions, tool position, and tool geometry, the CFA can be computed from an analytical modeling. As previously reminded, several models can be employed with more or less success. It has been shown in a preceding work that **C**- and **W**-models reveal good prediction capabilities regarding experimental CFA [13]. These two models were independently selected in our work to compute the CFA.
- **Step A-2** The present approach is based on the introduction of an equivalent uncut chip thickness h_{eq} deduced from the CFA η (the angle between the perpendicular to the cutting edge and the main flow direction of the chip). As illustrated in Fig. 2, in the case of straight turning with a zero approach angle, h_{eq} was assumed in this work given by the thickness of the uncut chip cross section along the chip flow direction passing by the tool nose center O at revolution position $n+1$. From a geometrical analysis, one has:

$$h_{\mathrm{eq}} = r_\varepsilon + f\cos(\eta) - \left[r_\varepsilon^2 - f^2\sin^2(\eta)\right]^{1/2}, \qquad (1)$$

since η was assumed ranging between 0 and $\pi/2$.
- **Step A-3** 2D cutting forces in the u and v direction, see Fig. 2, can be calculated adopting a plane strain configuration. Analytical or numerical means could be used for this stage. It is possible to introduce advanced analytical models, as the Li et al. [20] model, based on the unequal division shear-zone to predict the 2D cutting force components, or more complex analytical 2D model that takes into account the tool wear effect on the amount of the cutting force (e.g., Sun et al. [21]). In this work, numerical simulations were conducted in plane strain configuration with h_{eq} as an input parameter. Computed forces are denoted by F_u^{num} and F_v^{num} corresponding to cutting forces in the plane (u, v), see Fig. 2.
- **Step B-1** For the purpose of the analysis, the uncut chip cross section S need to be determined. It is derived from geometrical analysis with two situations. By taking into consideration the case where the approach and inclination angles are equal to zero, two configurations can be met:
  - $d \geq r_\varepsilon$: in this case (depicted in Fig. 3a), S is given by:

$$S = f(d - r_\varepsilon) + \int_{\theta_1}^{\pi} \frac{1}{2} h(\theta)\left[2r_\varepsilon - h(\theta)\right] d\theta\,, \qquad (2)$$

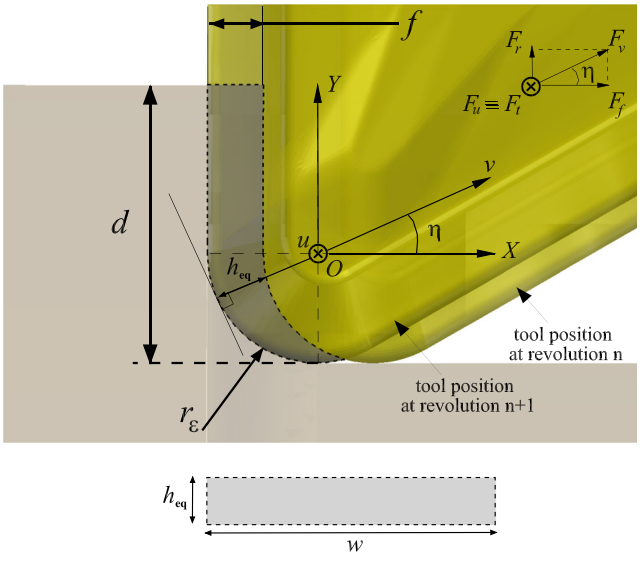

Fig. 2 Illustration (when $d > r_\varepsilon$) of the chip flow angle η and definition of the equivalent uncut chip thickness h_{eq}. The width of cut w is deduced from the ratio between the uncut chip area S (*dashed box* on the turning configuration equivalent to the *dashed rectangle*) and h_{eq}

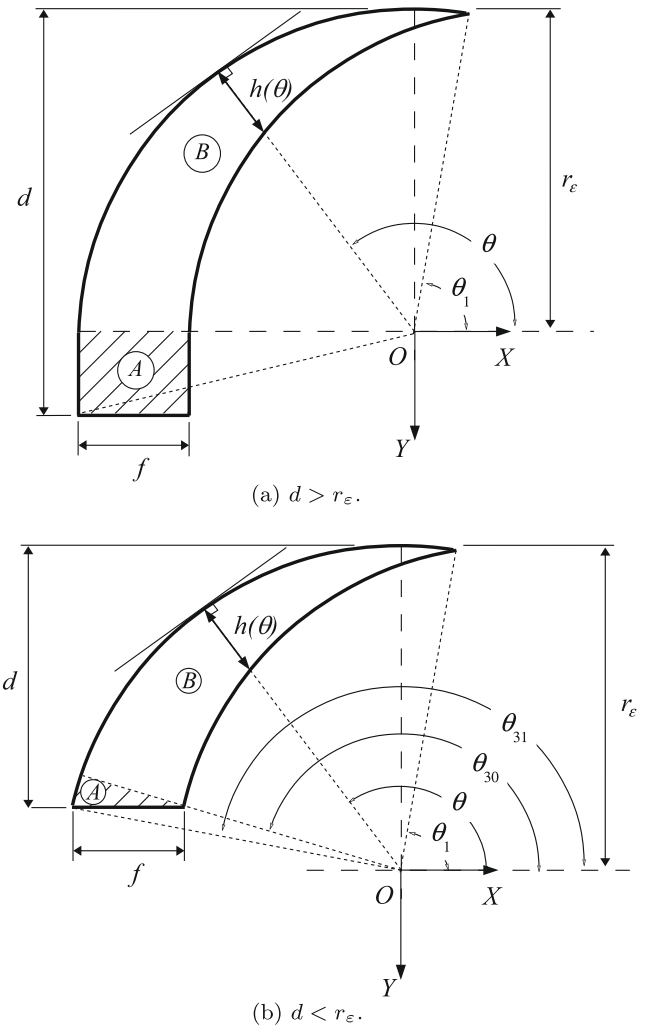

Fig. 3 Two cases of cutting conditions **a** $d > r_\varepsilon$ and **b** $d < r_\varepsilon$

with:

$$h(\theta) = r_\varepsilon - f\cos(\theta) - \left[r_\varepsilon^2 - f^2\sin^2(\theta)\right]^{1/2}. \tag{3}$$

◇ $d < r_\varepsilon$: in this case (illustrated in Fig. 3b), S is given by:

$$S = \int_{\theta_1}^{\theta_{31}} \frac{1}{2} h(\theta)\left[2r_\varepsilon - h(\theta)\right] d\theta\,, \tag{4}$$

where $h(\theta)$ is expressed as:

$$h(\theta) = r_\varepsilon - f\cos(\theta) - \left[r_\varepsilon^2 - f^2\sin^2(\theta)\right]^{1/2} \tag{5}$$

for $\theta_1 \leq \theta \leq \theta_{30}$ and

$$h(\theta) = r_\varepsilon - \frac{r_\varepsilon - d}{sin(\theta)} \tag{6}$$

for $\theta_{30} \leq \theta \leq \theta_{31}$.

Angles used in preceding equations are given by:

$$\theta_1 = \arccos\left(\frac{f}{2r_\varepsilon}\right), \tag{7a}$$

$$\theta_{30} = \pi - \arctan\left[\frac{r_\varepsilon - d}{\left(2r_\varepsilon d - d^2\right)^{1/2} - f}\right], \tag{7b}$$

$$\theta_{31} = \pi - \arcsin\left[\frac{r_\varepsilon - d}{r_\varepsilon}\right]. \tag{7c}$$

Note that when $r_\varepsilon = d$, zone A on Fig. 3b vanishes and $\theta_{30} = \theta_{31} = \pi$, such that $h(\theta)$ is obtained in an equivalent manner from Eq. 3 or Eq. 5. Note also that the equivalent uncut chip thickness given by Eq. 1 is retrieved using Eq. 3 or 5 with $\theta = \pi - \eta$, such that $h_{\text{eq}} = h(\theta = \pi - \eta)$.

– **Step B-2** It was assumed that the undeformed chip cross section S defined in the description of the cutting process is preserved when considering a plane strain process. As a consequence, the two areas on Fig. 2 (dashed box on the turning configuration and dashed rectangle) are equivalent such that the width of cut w was deduced from the ratio between the uncut chip area S and h_{eq} by:

$$w = \frac{S}{h_{\text{eq}}} \tag{8}$$

– **Step C** The last stage is to asses the three components of the resultant cutting force. In the plane (X, Y), the force F_v is the resultant force of the two components F_f and F_r. Note also that numerical simulations were computed in plane strain configuration with a depth of cut of 1 mm (value by default). As a consequence, following relationships were retained, see Fig. 2:

$$F_t = F_u = \tilde{w} F_u^{\text{num}} \tag{9a}$$

$$F_f = \cos(\eta) F_v = \tilde{w}\cos(\eta) F_v^{\text{num}} \tag{9b}$$

$$F_r = \sin(\eta) F_v = \tilde{w}\sin(\eta) F_v^{\text{num}} \tag{9c}$$

with $\tilde{w} = w/1$ mm the dimensionless depth of cut.

2.2 Modeling of the chip flow angle

We adopted the **W**-model [9] and the **C**-model [7] for their simplicity and their often use in predicting the CFA. Also, as shown in a preceding work [13], this two modelings may stand as upper and lower bounds of the experimental CFA. Equations relative to general turning configurations were fully addressed in the work of Wang [9]. For sake of consistency, it is just reminded here the **W**-model in the case where $(i, C_s) = (0, 0)$. This case corresponds to experimental tests that were used in the validation stage of the proposed modeling. However, the approach can be adapted to cases with more general cutting conditions, if one takes care of using projected angles in the equivalent cutting plane (e.g., see Wang [9] for more details).

2.3 **W**-model

In the work of Wang [9], the undeformed chip section is seen as a series of infinitesimal elements, each identified by its angular position θ, see Fig. 4. The elemental friction force $\underline{dF}$ is supposed deviating from the direction of the undeformed chip element by the tool local inclination angle $i_r(\theta)$, as shown in Fig. 4. In the **W**-model, the chip flow

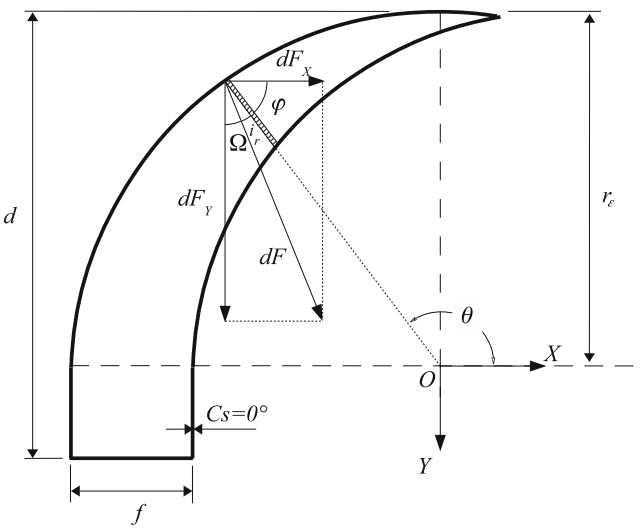

Fig. 4 **W**-model of chip flow direction. Chip flow and friction force at nose radius edge

angle is measured from the normal to the straight major cutting edge of the tool in the rake face plane. It is given by, in the case where $(i, C_s) = (0, 0)$:

$$\eta = \frac{\pi}{2} - \arctan\left(\frac{\int \sin\Omega \, dA}{\int \cos\Omega \, dA}\right), \tag{10}$$

where Ω, the angle made by $\underline{dF}$ with the positive Y axis, is given by:

$$\Omega = \begin{cases} \frac{\pi}{2} - i_r(\theta) - \varphi = \pi - i_r(\theta) - \theta, & \text{for } \theta \le \pi \\ 0, & \text{for } \theta \ge \pi \, . \end{cases} \tag{11}$$

$\varphi = \theta - \pi/2$ stands for the angle made by the positive X axis direction with the undeformed chip element, see Fig. 4. In the course of the **W**-model derivation, when $(i, C_s) = (0, 0)$, the local inclination angle in the tool nose is given in terms of the angular position θ by, see Fig. 4:

$$i_r(\theta) = -\arcsin(\sin\theta \sin\alpha) \, . \tag{12}$$

From Eq. 12, it can be noticed that $i_r(\theta)$ may be affected by the normal rake angle. On the straight major cutting edge, the rake angle has no effect since it is given by the global cutting inclination angle (zero here). No more details are given concerning the **W**-model since it is well documented in the literature (e.g., see [9, 13]).

2.4 C-model

In the **C**-model, the CFA is obtained from the perpendicular to the major cutting edge to the perpendicular to the line AB connecting the two end points of the uncut area, see Fig. 5. Making use of the geometry of Fig. 5, it can be found:

$$\eta = \begin{cases} \frac{\pi}{2} + \psi - \theta_1, & \text{if } d \ge r_\varepsilon \\ \arctan\left[\frac{\sqrt{2r_\varepsilon d - d^2} + f/2}{d - r_\varepsilon(1 - \sin\theta_1)}\right], & \text{if } d \le r_\varepsilon \end{cases} \tag{13}$$

with

$$\begin{aligned} \psi &= \arcsin\left[\frac{OA}{AB}\sin(\theta_2 - \theta_1)\right] \\ \theta_1 &= \arccos\left(\frac{f}{2r_\varepsilon}\right) \\ \theta_2 &= \pi + \arctan\left(\frac{d - r_\varepsilon}{r_\varepsilon}\right) \\ OA &= \sqrt{(d - r_\varepsilon)^2 + r_\varepsilon^2} \\ AB &= \sqrt{OA^2 - 2r_\varepsilon OA\cos(\theta_2 - \theta_1) + r_\varepsilon^2} \, . \end{aligned} \tag{14}$$

3 Experimental procedure

3.1 Machined material and tool characteristics

The workpiece was made of 304L austenitic stainless steel with chemical composition detailed in Table 1.

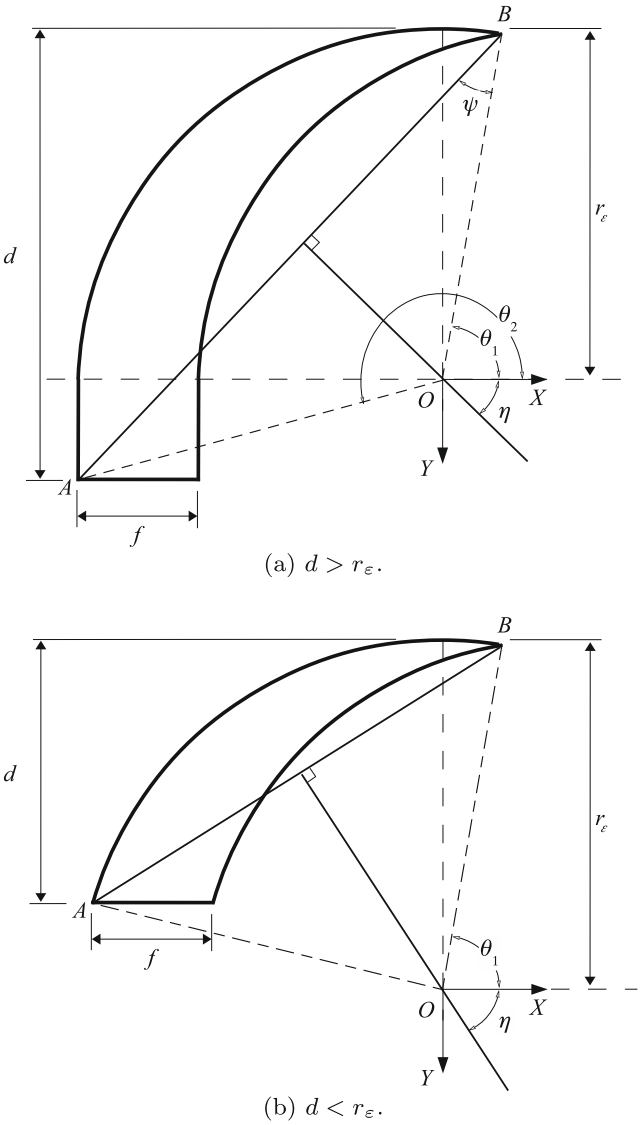

Fig. 5 **C**-model of chip flow direction. The CFD is perpendicular to the line connecting the two end points of the uncut chip cross section in the case where **a** $d > r_\varepsilon$ and **b** $d < r_\varepsilon$

This material was in the form of rods of circular cross section (radius 50 mm, length 120 mm) and was machined with a Mazak's Quick Turn Nexus turning center without using any lubrication. Time-series profiles of the acquired force data revealed relatively constant values over the length of cut and vibrations were limited.

The tool holder was a Sandvik Coromant referenced STGCL2525M16 and the cutting tool, designated as

Table 1 Chemical composition of the studied 304L stainless steel (in wt. %)

Alloy	*C*	*Si*	*Mn*	*P*	*S*	*Ni*	*Cr*	*N*
304L	0.017	0.354	1.095	0.030	0.023	8.091	18.156	0.084

TCMT16T308, was a WIDIA triangular shape insert (see Fig. 6) with the nose radius r_ε equals to 0.8 mm. The tool material was a coated WC-Co carbide made of MT-CVD/PVD TiN-Al2O3-TiCN-TiN coating layers (referred to as TN7110 by the tool manufacturer WIDIA). A similar coating was previously analyzed, and its thermomechanical behavior was studied through numerical simulations by Koné et al. [17]. Also, more details of conducted experiments were previously published [13].

3.2 Experimental set-up and cutting conditions

Experiments were conducted under dry condition. The lead angle C_s and the tool inclination angle i were set to $(C_s, i) = (0, 0)$. The three components of the resultant force, F_t, F_f, and F_r standing for tangential, feed, and radial component force, respectively, were captured using a Kistler $9129AA$ multicomponent dynamometer.

The aim of the present work is not to cover a total map of cutting conditions for the considered tool/workpiece combination. As a consequence, not large range of cutting conditions has been explored. Rather a constant cutting velocity V = 100m/min was imposed and two sets of cutting conditions were considered: a constant depth of cut d = 1mm with a feed rate f varying from 0.05 to 0.35 mm/rev and a constant feed rate f = 0.15 mm/rev with a depth of cut varying from 0.2 to 3 mm. That may cover some finishing to roughing operations.

4 Geometric modeling of the cutting tool

4.1 3D digitization procedure

This section deals with the 3D-digitization of the cutting tool and the post-process that leads to the identification of the 2D-section used in numerical simulations.

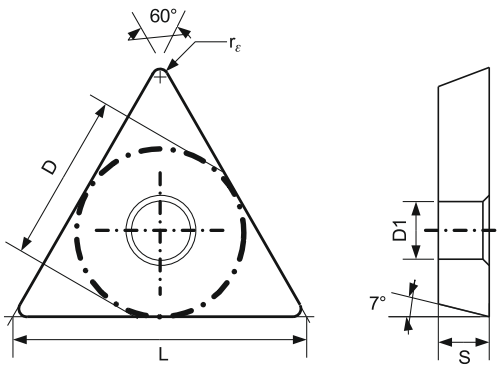

Fig. 6 TCMT16T308 cutting tool characteristics (dimensions are in *mm*) L = 16.5, D = 9.53, $D1$ = 4.4, S = 3.97, r_ε = 0.8

4.1.1 Experimental measuring system

The digitization of the cutting tool was done with a Breuckmann optoTOP-HE™coded structured light system. The system consisting of a camera and an active light source is based on special projection patterns combining Gray code and phase shifting, see Fig. 7. Some technical specifications associated to the digitization system are provided in Table 2. For any further information, the interested reader may refer to the work of Akca et al. [22] who used a similar Breuckmann system in the field of cultural heritage applications or Salvi et al. [23] where an exhaustive survey of coded structured light techniques used for 3D measurement is presented.

4.1.2 Digitization of the TCMT16T308 groove cutting tool

Prior to the digitization itself, a white powder was sprayed on the cutting tool in order to limit the sample reflectance and to facilitate the acquisition operation. This preparatory step was carefully done to limit surface inhomogeneities induced by deposited powder coating.

The whole object was covered with 14 scans, and each scan composed of 1.2 million points. The associated software of the measuring system (OPTOCAT™) was used to merge all scans and reduce the total number of points in

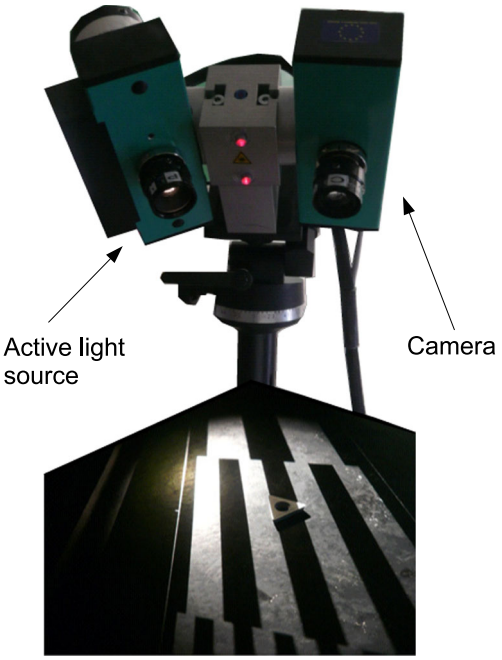

Fig. 7 Topometric system. The active light source illuminates the sample with a sequence of Gray coded binary fringe patterns. A 1.4 MPixel color camera and a field of view of 50 × 40 *mm* have been used

Table 2 Technical specifications of optoTOP-HE™sensor

Field of view (mm)	50 × 40
Depth of view (mm)	20
Acquisition time (s)	≃ 1
Feature accuracy (μm)	±6

the point cloud. As a result, a combined polygon mesh (merging) was generated consisted of approximately 240,000 triangles and 120,000 points (measuring precision of about 6 µ m from manufacturer's data). Figure 8 shows the three-dimensional acquisition of the cutting tool (final points cloud) illustrating different scans (in different colors) that have been merged. A CAD model reconstruction has been performed where only the rounded edge radius was imposed to a value of 0.1 mm (evaluated from the measured mean value) in order to avoid any difficulties that might emerge from numerical simulations.

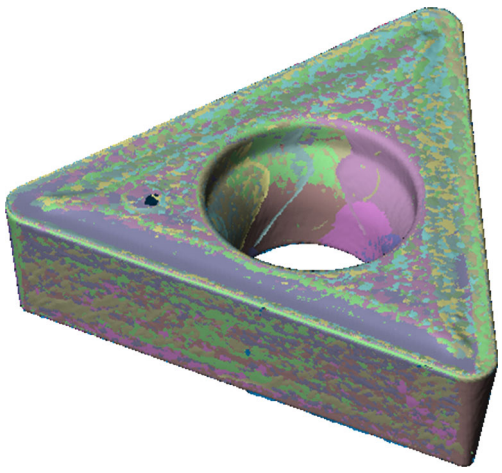

Fig. 8 Three-dimensional data acquisition of the cutting tool: point cloud acquired from the structured light system with approximately 120,000 single points as a virtual representation of the tool

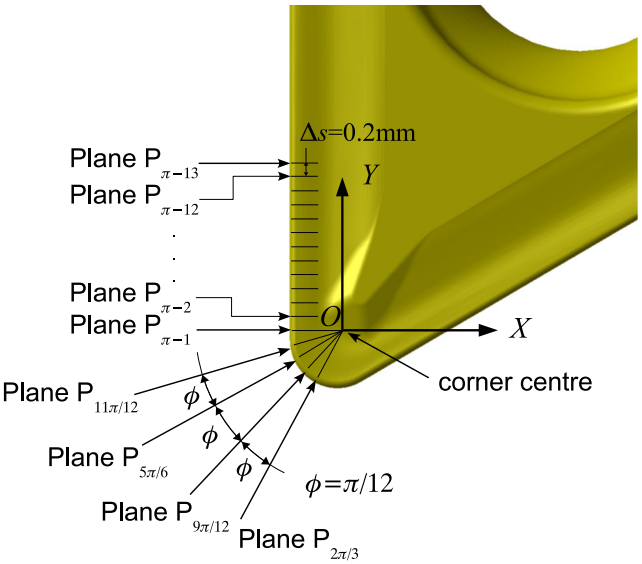

Fig. 9 Three-dimensional cutting tool and defined cutting planes from which sketches are extracted

4.2 2D profile extraction

The cutting tool was carefully examined along the cutting edge where the 2D cross section may vary from one position to another. Several cutting planes (orthogonal to the cutting edge) have been defined in the nose radius and in the straight edge, see Fig. 9. Corresponding 2D profiles that were extracted from the CAD model exhibit a typical shape, as schematically depicted on Fig. 10 where α_p and r_β stand for the local prior rake angle (measured close to the tool tip) and the corner radius. Remind that the latter was set at a value of 0.1 mm during the reconstruction step. The clearance angle, denoted by γ, is equal to $\sim 9°$ (somewhat different from the expected value) for all sections. The parameter δ in Fig. 10 is introduced in order to describe the chip breaker design.

Figure 11 shows the change in α_p (left vertical axis) and δ (right vertical axis) along the cutting edge when varying the edge length s. Note that evolutions are symmetrical about the vertical line passing through $s = 0$ that refers to the location where the plane $P_{2\pi/3}$ intersects the edge curve, see Fig. 9. Regarding the prior rake angle α_p, Fig. 11 broadly reveals two main regions within which α_p is slightly varying. In the tool nose, α_p is lying between 5 and 6.7° with a kind of valley in the vicinity of $s = 0$, whereas in the major or minor cutting edge, its value is about 8°. The chip breaker index δ variation along the edge curve follows a little different trend. It suffers from a rapid variation in the vicinity of $s = 0$ that is due to the increasing gap between the nose cutting edge and the protrusion edge on the tool

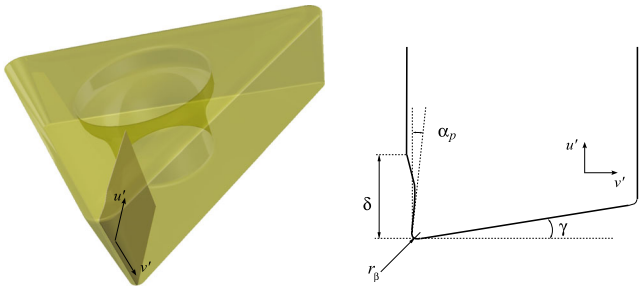

Fig. 10 Three-dimensional cutting tool and sketch of a typical 2D-section (orthogonal to the cutting edge). The extracted 2D profile corresponds to plane $P_{2\pi/3}$, see Fig. 9. For this illustrated profile, $\alpha_p = 6°$, $\gamma = 9°$, $r_\beta = 0.1$ mm, and $\delta = 1.2$mm

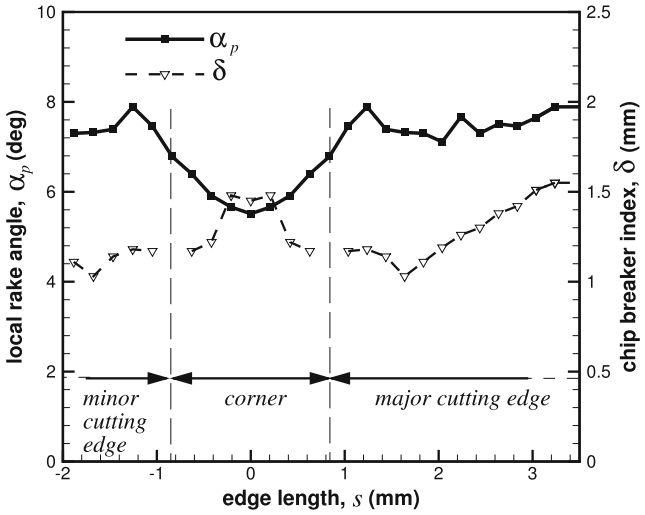

Fig. 11 Local prior angle α_p *(left vertical axis)* and chip breaker index δ *(right vertical axis)* versus the edge length s along the edge curve. The intersection of the tool with plane $P_{2\pi/3}$ defines the location where $s = 0$

insert (see also Fig. 9), and it is linearly increasing in the major (resp. minor) cutting edge as s is increased (resp. decreased). Note also on Fig. 11 that two values of δ are missing for $s = 0.84$ and $s = -0.84$ mm where no evidence of chip breaker specificity has been noticed. This can be explained by the location of the corresponding cutting plane P_{π_1} that passes at the basis of the protrusion edge (see also Fig. 9).

As previously mentioned, our modeling is based on 2D numerical simulations with an equivalent uncut chip thickness deduced from the CFA which in turn depends on cutting conditions. Following a rigourously same point of view, it would have been necessary to consider in numerical simulations a 2D tool profile corresponding to each calculated uncut chip thickness. However, to the authors point of view, this induces complexity in using the proposed approach and might not be as useful as expected. Indeed, since the CFA is ranging from 0 to $\pi/2$, the corresponding 2D section must lie in the tool corner where it has been observed that even if some variations are observed in α_p and δ, they are limited and the profile appears to be similar along the rounded edge. As a consequence, a single 2D section is adopted for all numerical simulations and is chosen as extracted from the intersection of the three-dimensional CAD with the cutting plane $P_{2\pi/3}$. The geometry is given in Fig. 10.

5 Finite element modeling

Finite element software DEFORM was used to complete step A-2 shown in the synoptic diagram, see Fig. 1. This stage was done to perform cutting simulations under 2D plane strain assumption and to provide regression relationships of F_x^{num} and F_y^{num} as functions of the equivalent undeformed chip thickness h_{eq}. The coated cutting tool is considered as thermo-rigid body. The machined part is assumed thermo-elastic-viscoplastic. Constitutive behavior of insert, coatings, and workpiece materials are taken from the DEFORM package [24]. The geometry and the mesh of the workpiece and of the coated tool are illustrated in Fig. 12a. The tool geometry is also depicted in Fig. 10. The workpiece is meshed with about 3000 quadrilateral linear finite elements and the tool with about 1300 elements of the same type. The mesh is refined in the vicinity of the tool chip interface where the mesh size is approximately 10–15μ m. In order to prevent excessive distortion of elements, automatic remeshing is triggered when the interference depth of the tool nodes in the mesh of the workpiece reaches a specified value (30μ m). Thicknesses of each coating layer, reported in Fig. 12b were estimated from optical observations.

5.1 Cutting and boundary conditions

A cutting velocity of 100 m/min is applied to the bottom line of the workpiece while the insert is considered fixed. Thermal boundary conditions are illustrated in Fig. 13 where three regions are defined. In a preceding work of the authors [17], the thermal problem was addressed in a same manner through numerical simulations and basic

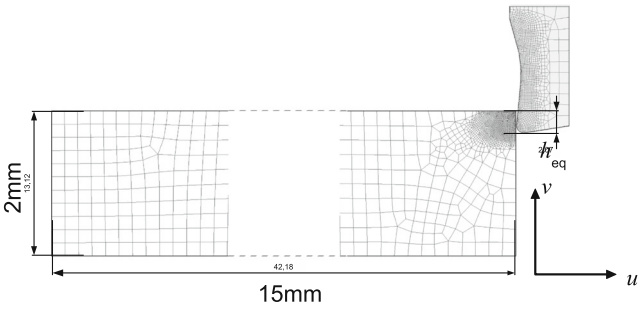

(a) 2D plane strain configuration.

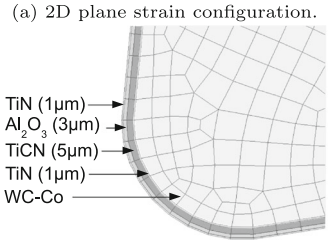

(b) Multilayer coated tool.

Fig. 12 **a** Geometry, initial mesh, and dimensions considered in numerical simulations. The tool is fixed while the workpiece is moving at a velocity of 100 m/min. The undeformed chip thickness h_{eq} is an input data. **b** The different coatings thicknesses have been estimated from optical observations

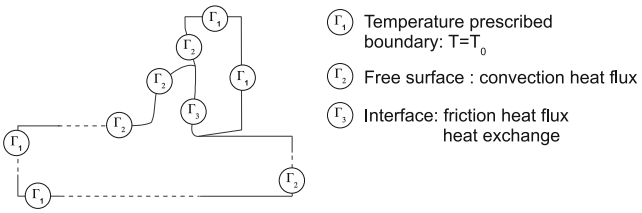

Fig. 13 Thermal conditions used in numerical simulations [17]

equations when considering different coating layers of a tungsten carbide tool machining an austenitic steel. Effects of coatings on pressure and temperature distributions at the contact area as well as temperature gradients within the tool bulk were compared, and coating effects have been underlined. Same conditions are considered here where the left and bottom boundaries of the workpiece, as the top and right boundaries of the tool, are assumed to be maintained at a constant temperature $T_0 = 20$ °C, zone Γ_1 in Fig. 13. Thermal exchanges between the workpiece and the environment (zone Γ_2 in Fig. 13) are accounted for with a convective heat transfer coefficient of 20 $\mathrm{Wm^{-2}K^{-1}}$. Zone Γ_3 in Fig. 13 refers to thermal interaction between the tool and the chip. Heat fluxes within the contacting solids are driven by the heat friction (managed by the friction coefficient μ) and the heat conduction between the tool and the workpiece (controlled by the heat transfer coefficient h). The first heat source is assumed here governed by a Coulomb model (coefficient of friction μ = 0.5) where the friction stress is limited by the shear flow stress. The second heat source is accounted for by adopting a constant value $h = 10^6 \mathrm{Wm^{-2}K^{-1}}$, based on the work of Yen et al. [16] and Koné et al. [17].

5.2 Material parameters

5.2.1 Constitutive behavior of the workmaterial

Different material data are available in the DEFORM package [24] through strain-stress curves at different temperatures and strain rates. It is well known that for a given material, a large number of behavior descriptions (several constitutive laws, different parameters for a given law) can be found in the literature. In the present study, since the finite element software do not provide the 304L steel database, it was considered the behavior of the corresponding 304 austenitic steel available in the DEFORM package [24]. Thus, the stainless steel was assumed to follow similar major trends than the low-carbon corresponding alloy regarding thermomechanical response to different loading conditions. To get an idea of the workmaterial behavior considered in numerical simulations, a least square method based on DEFORM adopted strain-stress curves was used to identify the Johnson Cook [25] constitutive law. This law, purely phenomenological, was originally proposed by the authors for computational convenience. A large range of materials (OFHC copper, 4340 Steel, Tungsten alloy...) were then considered and impact tests on cylinder bars were used in the validation step. Adopting this constitutive law, the flow stress can be expressed as:

$$\bar{\sigma} = g(\bar{\varepsilon})h\left(\dot{\bar{\varepsilon}}\right)k(T) \tag{15}$$

with

$$g\left(\bar{\varepsilon}\right) = A + B\bar{\varepsilon}^n \tag{16a}$$

$$h\left(\dot{\bar{\varepsilon}}\right) = 1 + C\ln\left(\frac{\dot{\bar{\varepsilon}}}{\dot{\bar{\varepsilon}}_0}\right) \tag{16b}$$

$$k(T) = 1 - \hat{T}^m, \quad \hat{T} = \frac{T - T_{ref}}{T_{melt} - T_{ref}} \tag{16c}$$

where $\dot{\bar{\varepsilon}}$ is the equivalent plastic strain rate and $\bar{\varepsilon} = \int \dot{\bar{\varepsilon}} dt$ is the cumulative plastic strain. In Eq. 16a A is the yield stress when $T = T_{ref}$ and $\dot{\bar{\varepsilon}} = \dot{\bar{\varepsilon}}_0$, B and n are hardening parameters. Parameter C in Eq. 16b controls the strain rate sensitivity and $\dot{\bar{\varepsilon}}_0$ is a reference strain rate. In Eq. 16c, T_{melt} refers to the melt temperature and T_{ref} is a reference temperature, m is the thermal softening coefficient. Table 3 summarizes the set of identified Johnson Cook parameters.

5.2.2 Thermal and elastic properties of the workmaterial

Thermal conductivity λ, volumetric heat capacity ρc_p, linear thermal expansion coefficient α_T, and Young's modulus E of the AISI 304L considered in numerical simulations are temperature dependent following values of the 304 provided by DEFORM [24] and illustrated in Fig. 14. Poisson's ratio is 0.3.

5.2.3 Tool properties

The coated WC–Co carbide tool, made of MT-CVD /PVD TiN–Al2O3–TiCN–TiN coating layers, is assumed rigid. As a consequence, only thermal conductivities and volumetric heat capacity are relevant parameters. Adopted values referring to each coating and to the carbide are reported in Table 4.

Table 3 Material parameters used in numerical simulations

A (MPa)	B (MPa)	C	n	m	$\dot{\bar{\varepsilon}}_0$ (s^{-1})	T_{melt} (K)	T_{ref} (K)
437	428.5	0.0254	0.364	2.019		1700	293

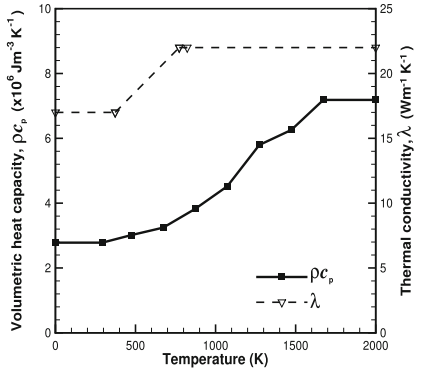

(a) Volumetric heat capacity ρc_p (left axis) and thermal conductivity λ (right axis) versus temperature.

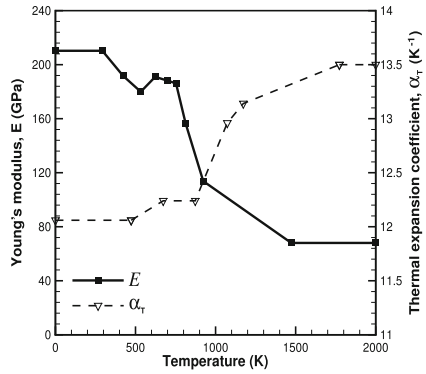

(b) Young modulus E (left axis) and thermal expansion coefficient α_T (right axis) versus temperature.

Fig. 14 Physical properties of the 304L considered in numerical simulations versus temperature

5.3 FE results and numerical forces relationships

From the proposed approach, it appears that for a given cutting velocity V_c, a given work and tool material combination with its 2D finite element implementation h_{eq} is the only input data need to obtain numerical cutting forces F_u^{num} and F_v^{num}. From these force components, F_r, F_t, and F_f are deduced for a set (f, d) of feed rate and depth of cut (see Eq. 9). As a consequence and for a convenient use of our approach, different values of the equivalent uncut chip thickness have been considered in numerical simulations to identify regression relationships $F_u^{\text{num}}\left(h_{\text{eq}}\right)$ and $F_v^{\text{num}}\left(h_{\text{eq}}\right)$.

In a same way as Afazov et al. [26] established a relation between cutting forces and uncut chip thickness in a finite element modeling of orthogonal cutting, a two-phase exponential relation has been adopted here. This was done to capture the non-linearity at small uncut chip thicknesses as well as a potential non-linearity at large uncut chip thicknesses. The adopted relationship is expressed as:

$$F_{u,v}^{\text{num}} = p_1\left[1-\exp\left(p_2 h_{\text{eq}}\right)\right] + p_3\left[1-\exp\left(p_4 h_{\text{eq}}\right)\right], \tag{17}$$

where p_i, $i = 1\ldots4$, are parameters to be determined for each force. Figure 15 shows numerical forces obtained for h_{eq} = 0.04, 0.1, 0.15, 0.2, and 0.25 mm and forces given by relation (17) and parameters listed in Table 5. The cutting velocity was 100m/min. The fundamental need here was to describe as well as possible the evolution of numerical forces F_u^{num} and F_v^{num} as functions of the undeformed chip thickness. This was done with a good accuracy by considering (17) with parameters listed in Table 5.

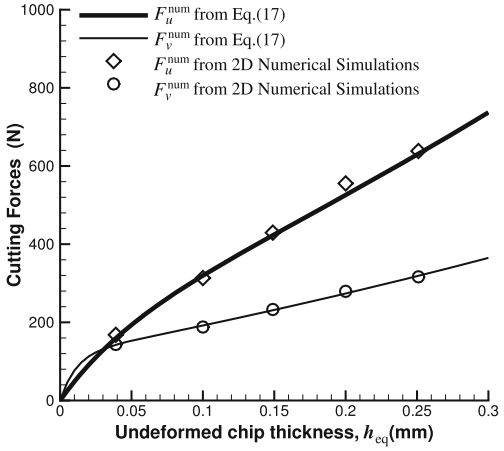

Fig. 15 Comparison between cutting forces computed from 2D numerical simulations and values obtained from Eq. 17

6 Comparison with experiments

In this section, experimental cutting forces are compared to values obtained from the proposed approach. As previously mentioned, step-A1 in Fig. 1 was solved by considering

Table 4 Carbide and coating properties considered in numerical simulations from [24]

	WC–Co	TiN	TiCN	Al2O3
ρc_p $(10^6 Jm^{-3}K^{-1})$	15	12	15	3.43
λ $(Wm^{-1}K^{-1})$	59	25	30	7.5

Table 5 Identified parameters and coefficient of determination obtained in force components empirical relationships (17). Cutting velocity was 100 m/min

	p_1	p_2	p_3	p_4	R^2
F_u^{num}	177.3	−20.3	−1346	1.16	0.992
F_v^{num}	118.2	−89.4	−659	1.06	0.997

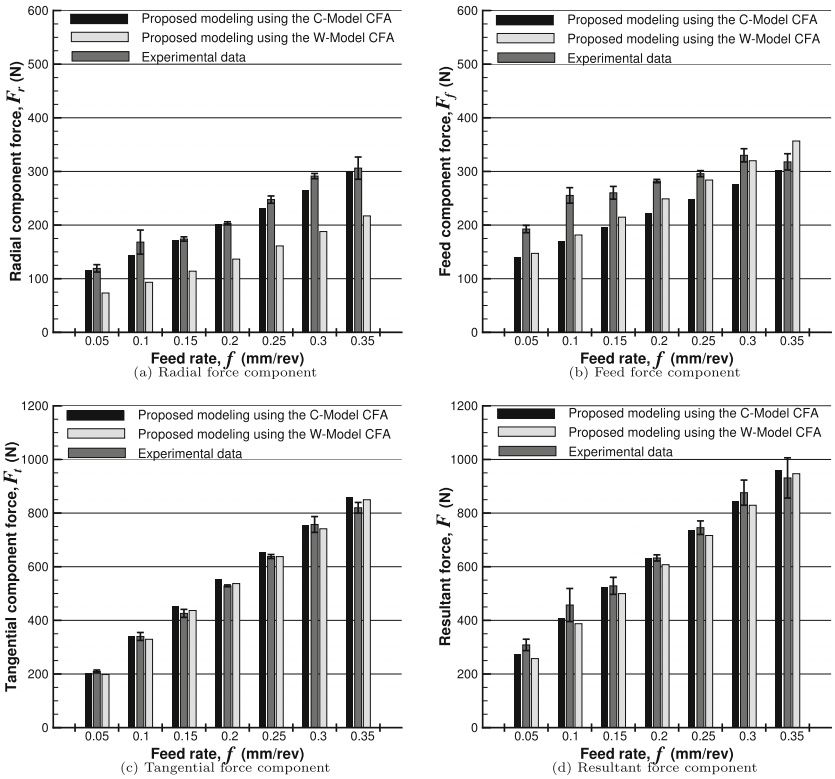

Fig. 16 Experimental forces versus feed rate and corresponding standard deviations of the mean value compared to computed forces from the proposed approach. The depth of cut is 1 mm

two CFA modelings. The proposed approach is therefore first discussed in terms of the influence of the chosen CFA modeling.

6.1 Varying feed rate

Figure 16 shows evolutions of cutting forces versus the feed rate for a depth of cut of 1 mm and a cutting velocity of 100m/min. One can observe that major trends are retrieved by the proposed approach when using any of the CFA modelings used to solve step-A2. An increase in the feed rate leads to an increase in all force components. This statement has been largely discussed in the literature. As shown in [13, 27], CFA predicted by the Wang's modeling leads to lower values than those evaluated from the Colwell's approach. As seen in Eq. 1, in our approach, that inevitably leads to larger equivalent uncut chip thicknesses when using the Wang's CFA prediction. However, even if chip flow angles may reveal great discrepancies, differences in h_{eq} are very limited explaining why tangential cutting forces are similar when Colwell or Wang's CFA is considered, see Fig. 16c. Indeed, tangential force is proportional to the numerical force F_u^{num}, see Eq. 9a. With near same values of h_{eq} and $\tilde{w}$, similar tangential component forces are expected. More differences can be observed when feed or radial forces are investigated, see Fig. 16a, b. From Eqs. 9b and c, it appears that a lower value of the CFA leads to a greater radial force component and a lower feed force component, noting that the sine (resp. cosine) function is monotonically increasing (resp. decreasing) in the range of possible argument $0° \leq \eta \leq 90°$. As a consequence, computed feed forces obtained from the modeling with the Wang's CFA are lower than those computed with the Colwell's CFA. In this respect, Table 6 summarizes predicted Wang and Colwell's

Table 6 CFA computed from **C**-model and **W**-model and corresponding uncut chip thicknesses. The depth of cut is fixed to d =1 mm and the feed rate f is varying

	$f(mm/rev) \rightarrow$	0.05	0.10	0.15	0.20	0.25	0.30	0.35
C-model	$\eta(°)$	39.5	40.4	41.3	42.2	43.1	43.9	44.8
	$h_{\text{eq}}(mm)$	0.039	0.078	0.119	0.160	0.201	0.244	0.287
W-model	$\eta(°)$	26.5	27.2	28.0	28.8	29.6	30.4	31.3
	$h_{\text{eq}}(mm)$	0.045	0.089	0.136	0.181	0.227	0.273	0.320

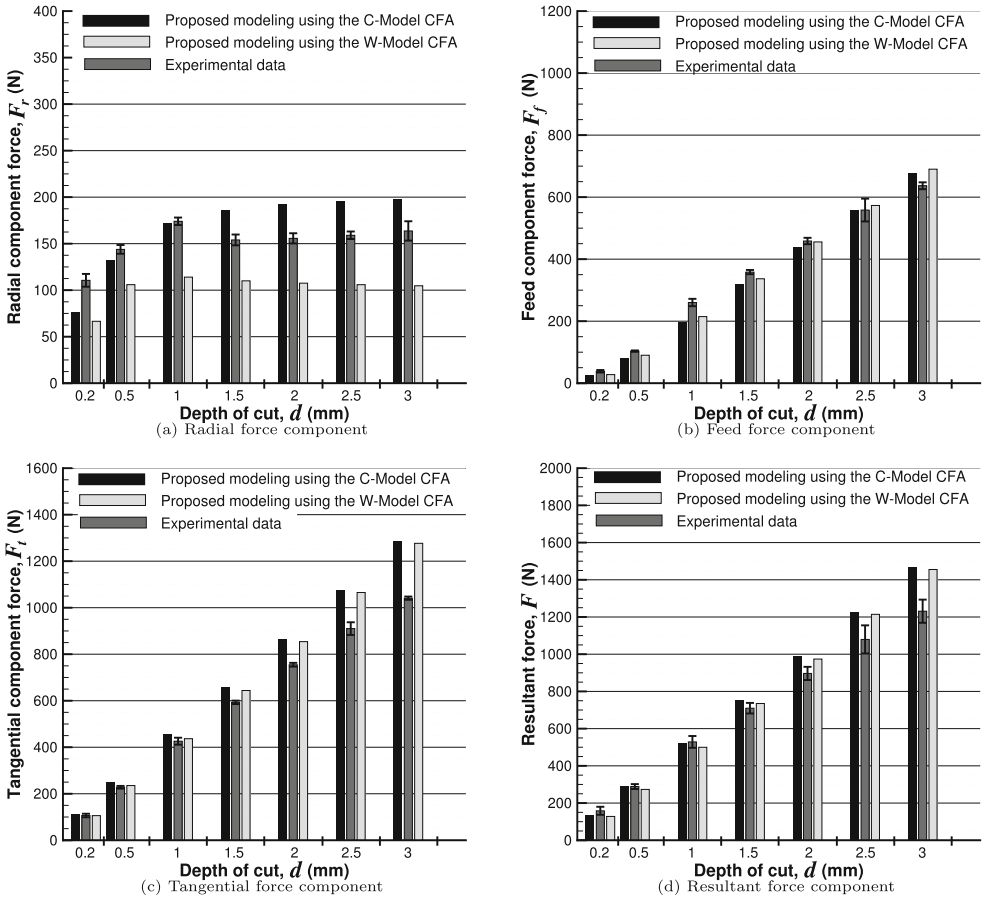

Fig. 17 Experimental forces versus depth of cut and corresponding standard deviations of the mean value compared to computed forces from the proposed approach. The feed rate is 0.15 mm/rev

CFA as well as corresponding undeformed chip thicknesses obtained from Eq. 1.

More generally, Fig. 16 shows that our approach predicts with a relatively good accuracy experimental data on a large range of feed rates. Tangential and resultant forces are well reproduced by our approach, when adopting any of the two CFA's modeling. Experimental feed force components are notably better described when the Colwell's CFA is accounted for. Most discrepancies are observed when comparing radial force components. From experiments, it is observed a small decrease in F_f as f is decreased while our approach, even if reproducing the tendency, appears to be more sensitive.

6.2 Varying depth of cut

The attention is now paid on the evolution of cutting forces for a constant feed rate $f = 0.15$ mm/rev and a varied depth of cut, see Fig. 17. Once again, usual major trends are retrieved with our approach. Differences obtained when using Wang's CFA and Colwell's CFA has been addressed in the preceding section and explanation still stands here. The value of the CFA mainly controls levels of F_f and F_r. Here, however, only the radial force component is sensitive to the CFA, particularly for depth of cut greater than 1 mm, see Fig. 17a. For low depth of cut, the gap between Wang's and Colwell's CFA is limited (less than 5° for $d = 0.2$ mm), see Table 7. As a result, the feed and radial forces are expected

Table 7 CFA computed from **C**-model and **W**-model and corresponding uncut chip thicknesses. The feed rate is fixed to 0.15 mm and the depth of cut d is varying

	$d(mm) \rightarrow$	0.2	0.5	1	1.5	2	2.5	3
C-model	$\eta(°)$	72.0	58.7	41.3	30.3	23.7	19.3	16.3
	$h_{eq}(mm)$	0.059	0.088	0.119	0.133	0.140	0.143	0.145
W-model	$\eta(°)$	67.4	49.6	28.0	18.1	13.3	10.5	8.6
	$h_{eq}(mm)$	0.070	0.105	0.136	0.144	0.147	0.148	0.148

to be similar. When the depth of cut is increased, the gap is also increased, and, moreover, the CFA is shifted downward where the sine function is highly sensitive to its argument. As an immediate consequence, the radial force obtained from Eq. 9c is very sensitive to the CFA.

Cutting forces obtained from our approach are compared with a reasonable good agreement to experimental data. Tangential forces seem, however, overestimated for large depth of cut. Again, experimental force components are notably better described when the Colwell's CFA is accounted for.

7 Conclusion

The present work deals with the development of a hybrid analytical/numerical approach dedicated to predict 3D cutting forces in turning. Numerical simulations, conducted in plan strain configuration, necessitate two key features: the tool geometry and the uncut chip thickness. The first is obtained from a 3D digitization procedure of the complex tool geometry. The second is deduced from the chip flow angle using an analytical formulation. To make the model as easy as possible to implement, computed numerical cutting forces are described by regression relationships. By this way, a complete map of 3D cutting forces can be drawn covering a large set of cutting conditions. The approach is aimed to be general enough to be applied to other machining processes by keeping a similar methodology. However, this should involve an adequate geometric analysis. Moreover, the modular aspect and the flexibility of the model makes it highly expandable. Each step of the proposed approach can be improved, revisited, or simplified (e.g., accounting for electrical, chemical, or coolant influences can proceed, as a first attempt, through the enrichment of the step-A3.).

A comparison with experimental cutting forces measured when machining an austenitic steel with a complex tool geometry reveals the good predictive capabilities of our approach. In the course of the derivation, two analytical modelings were chosen to solve the required chip flow angle. It has been shown that major trends are retrieved whatever the adopted modelings.

References

1. Merchant ME (1944) Basic mechanics of the metal cutting process. J App Mech 11:A168–A175
2. Yang K, Liang Y-C, Zheng K-N, Bai Q-S, Chen W-Q (2011) Tool edge radius effect on cutting temperature in micro-end-milling process. Int J Adv Manuf Technol 52:905–912
3. Adetoro OB, Wen PH (2010) Prediction of mechanistic cutting force coefficients using ALE formulation. Int J Adv Manufact Technol 46:79–90
4. Stabler GV (1951) The fundamental geometry of cutting tools. Proc Inst Mech Eng 165:14–21
5. Stabler GV (1964) The chip flow law and its consequences. In: 5th international machine tool design research conference, Birmingham, UK, pp 243–251
6. Russell JK, Brown RH (1966) The measurement of the chip flow direction. Int J Mach Tool Des Res 6:129–138
7. Colwell LV (1954) Predicting the angle of chip flow for single-point cutting tools. Trans ASME 76:199–204
8. Wang J, Mathew P (1995) Development of a general tool model for turning operations based on a variable flow stress theory. Int J Mach Tools Manufact 35(1):71–90
9. Wang J (2001) Development of a chip flow model for turning operations. Int J Mach Tools Manufact 41:1265–1274
10. Jawahir IS, Wang X (2007) Development of hybrid predictive models and optimization techniques for machining operations. J Mater Process Technol 185:46–59
11. Jawahir IS, Ghosh R, Balaji AJ, Li PX (2000) Predictability of tool failure modes in turning with complex grooved tools using the equivalent toolface (ET) model. Wear 244:94–103
12. Fang N, Wu Q (2009) A comparative study of the cutting forces in high speed machining of Ti-6Al-4V and Inconel 718 with a round cutting edge tool. J Mater Process Technol 209: 4385–4389
13. Koné F, Czarnota C, Haddag B, Nouari M (2013) Modeling of velocity-dependent chip flow angle and experimental analysis when machining 304l austenitic stainless steel with groove coated-carbide tools. J Mater Process Technol 213: 1166–1178
14. Deshayes L (2007) Analysis of an equivalent tool face for the cutting speed range prediction of complex grooved tools. J Mater Process Technol 190:251–262
15. Pereira RBD, Braga DU, Nevez FO, da Silva ASC (2013) Analysis of surface roughness and cutting force when turning AISI 1045 steel with grooved tools through Scott-Knott method. Int J Adv Manufact Technol 69:1431–1441
16. Yen YC, Söhner J, Lilly B, Altan T (2004) Estimation of tool wear in orthogonal cutting using the finite element analysis. J Mater Process Technol 146:82–91
17. Koné F, Czarnota C, Haddag B, Nouari M (2011) Finite element modeling of the thermomechanical behavior of coatings under extreme contact loading in dry machining. Surf Coat Technol 205:3559–3566
18. Soo SL, Dewes RC, Aspinwall DK (2010) 3D FE modelling of high-speed ball nose end milling. Int J Adv Manufact Technol 50:871–882
19. Özel T (2009) Computational modelling of 3D turning: Influence of edge micro-geometry on forces, stresses, friction and tool wear in PcBN tooling. J Mater Process Technol 209:5167–5177
20. Li B, Wang X, Hu Y, Li C (2011) Analytical prediction of cutting forces in orthogonal cutting using unequal division shear-zone model. Int J Adv Manufact Technol 54:431–443
21. Sun Y, Sun J, Li J, Li W, Feng B (2013) Modeling of cutting force under the tool flank wear effect in end milling Ti-6Al-4V with solid carbide tool. Int J Adv Manufact Technol 69:2545–2553
22. Akca D, Remondino F, Novák D, Hanusch T, Schrotter G, Gruen A (2007) Performance evaluation of a coded structured light system for cultural heritage applications. In: Videometrics IX, pp 29–30
23. Salvi J, Pagès J, Batlle J (2007) Pattern codification strategies in structured light systems. Pattern Recogn 37:827–849

24. Corporation Scientific Technologies (2008) DEFORM 2D, V9.1 User's manual. Columbus, OH
25. Johnson GR, Cook WH (1983) A constitutive model and data for metals subjected to large strains, high strain rates and high temperatures. In: Proceedings of the 7th international symposium on ballistics, The Hague, NL, pp 541–547
26. Afazov SM, Ratchev SM, Segal J (2010) Modelling and simulation of micro-milling cutting forces. J Mater Process Technol 210:2154–2162
27. Seethaler RJ, Yellowley I (1997) An upper-bound cutting model for oblique cutting tools with a nose radius. Int J Mach Tools Manufact 37:119–134